Foam generation in flow across a sharp permeability transition
Effect of velocity and fractional flow

Shah, Swej; As Syukri, Herru; Wolf, Karl Heinz; Pilus, Rashidah Mohd; Rossen, William R.

DOI
10.2118/195517-PA

Publication date
2019

Document Version
Final published version

Published in
Society of Petroleum Engineers - SPE Europec Featured at 81st EAGE Conference and Exhibition 2019

Foam Generation in Flow Across a Sharp Permeability Transition: Effect of Velocity and Fractional Flow

Swej Y. Shah, Herru As Syukri, Karl-Heinz Wolf, Delft University of Technology;
Rashidah M. Pilus, Universiti Teknologi Petronas; and **William R. Rossen,** Delft University of Technology

Summary

Foam reduces gas mobility and can help improve sweep efficiency in an enhanced-oil-recovery (EOR) process. For the latter, long-distance foam propagation is crucial. In porous media, strong foam generation requires that the local pressure gradient exceed a critical value ($\nabla P^{\min}$). Normally, this happens only in the near-well region. Away from wells, these requirements might not be met, and foam propagation is uncertain. It has been shown theoretically that foam can be generated, independent of pressure gradient, during flow across an abrupt increase in permeability (Rossen 1999). The objective of this study is to validate theoretical explanations through experimental evidence and to quantify the effect of fractional flow on this process.

This article is an extension of a recent study (Shah et al. 2018) investigating the effect of permeability contrast on this process. In this study, the effects of fractional flow and total superficial velocity are described. Coreflood experiments were performed in a cylindrical sintered-glass porous medium with two homogeneous layers and a sharp permeability jump in between, representing a lamination or cross lamination. Unlike previous studies of this foam-generation mechanism, in this study, gas and surfactant solution were coinjected at field-like velocities into a medium that was first flooded to steady state with gas/brine coinjection. The pressure gradient is measured across several sections of the core. X-ray computed tomography (CT) is used to generate dynamic phase-saturation maps as foam generates and propagates through the core. We investigate the effects of velocity and injected-gas fractional flow on foam generation and mobilization by systematically changing these variables through multiple experiments. The core is thoroughly cleaned after each experiment to remove any trapped gas and to ensure no hysteresis.

Local pressure measurements and CT-based saturation maps confirm that foam is generated at the permeability transition, and it then propagates downstream to the outlet of the core. A significant reduction in gas mobility is observed, even at low superficial velocities. Foam was generated in all cases, at all the injected conditions tested; however, at the lowest velocity tested, strong foam did not propagate all the way to the outlet of the core. Although foam generation was triggered across the permeability boundary at this velocity, it appeared that, for our system, the limit of foam propagation, in terms of a minimum-driving-force requirement, was reached at this low rate. CT images were used to quantify the accumulation of liquid near the permeability jump, causing local capillary pressure to fall below the critical capillary pressure required for snap-off. This leads to foam generation by snap-off. At the tested fractional flows, no clear trend was observed between foam strength and f_g. For a given permeability contrast, foam generation was observed at higher gas fractions than predicted by previous work (Rossen 1999). Significant fluctuations in pressure gradient accompanied the process of foam generation, indicating a degree of intermittency in the generation rate—probably reflecting cycles of foam generation, dryout, imbibition, and then generation. The intermittency of foam generation was found to increase with decreasing injection velocities and increasing fractional flow. Within the range of conditions tested, the onset of foam generation (identified by the rise in ∇P and S_g) occurs after roughly the same amount of surfactant injection, independent of fractional flow or injection rate.

Introduction

Foams have numerous applications in the oil industry. They are used for drilling (Lyons et al. 2009), to divert acids in well-stimulation procedures (Chambers 1994), for hydraulic fracturing of low-permeability formations (Gupta 2009), to improve liquid lifting in low-pressure gas wells (Yang and Siddiqui 1999), and for tertiary oil-recovery processes (Rossen 1996). In aquifer-remediation processes (Hirasaki et al. 1997a, 1997b, 2000), foam is used to improve sweep while removing dense nonaqueous-phase liquids. This work concerns using foam as a mobility-control agent in an EOR process.

Most of the world's EOR production comes from injecting gases. Gas has a low viscosity and density compared with oil and, therefore, in a displacement process, sweep efficiency is poor because of viscous fingering and gravity override. When used as a dispersed phase, as in foam, its apparent mobility is greatly reduced and sweep efficiency is improved. In a heterogeneous, layered system, as discussed by Tanzil et al. (2002a) and Shah et al. (2018), the effective permeability in the vertical direction could be greatly reduced by foam generation in the high-permeability strata, reducing the extent of gravity segregation. In porous media, foams can be generated in various ways (Ransohoff and Radke 1988; Kovscek and Radke 1994; Rossen 1996). Several experimental studies (Gauglitz et al. 2002; Tanzil et al. 2002b) and theoretical models (Rossen 1990a; Rossen and Gauglitz 1990; Friedmann et al. 1991; Kam and Rossen 2003) suggest that strong foam generation in porous media would require exceeding a critical pressure gradient or velocity threshold, which is typically only overcome in the near-well region. Creation of foam in these cases is thought to depend on mobilization of lenses and lamellae and subsequent lamella division. Mobilizing the bubble train requires a minimum pressure gradient (Rossen 1990a, 1990b; Kharabaf and Yortsos 1998; Chen et al. 2005; Almajid and Kovscek 2019). For CO_2 foams, this minimum pressure gradient might be so low at reservoir conditions (because of a lower interfacial tension) that it might not be observed in foam experiments.

Others argue that snap-off is the dominant mechanism of foam generation in a porous medium (Ransohoff and Radke 1988; Kovscek and Radke 1996, 2003). While snap-off can occur through several mechanisms (Rossen 2003), in these studies, the increased frequency of snap-off is thought to be dependent on pore geometry and interfacial curvature as well as gas-phase and liquid-phase velocities. The relevant mechanism of snap-off in these experiments is Roof snap-off (Roof 1970), which occurs as gas invades a narrow pore throat

This paper (SPE 195517) was accepted for presentation at the SPE Europec featured at the 81st EAGE Conference and Exhibition, London, UK, 3–6 June 2019, and revised for publication. Original manuscript received for review 13 December 2018. Revised manuscript received for review 25 June 2019. Paper peer approved 26 June 2019.

and drains liquid from a wider downstream pore body. These studies report no minimum-pressure-gradient requirement for foam generation but argue that snap-off might cease if the newly created lamellae or lenses cannot mobilize (Kovscek and Radke 1996). As mentioned earlier, the mobilization of lamellae from a snap-off site requires a minimum pressure gradient. Other research reporting similar findings was revisited by Almajid and Kovscek (2016). Foam experiments that start with a surfactant-saturated core, analogous to gas draining the preceding surfactant slug in a surfactant-alternating-gas flood in the near-well region, might not observe this critical velocity or pressure-gradient dependence. There appears to be no clear consensus in the literature on the most dominant mechanisms of strong-foam generation in porous media. In this study, we are interested in foam-generation mechanisms that could dominate away from wells, where the pressure gradient is low and the Darcy velocity is considered to be, in practice, approximately 1 ft/D (Dake 1994)—much lower than the reported thresholds in the studies referred to previously. These are regions where the gas and surfactant slugs injected into a reservoir would have mixed, and gas is not draining a surfactant-saturated zone.

If strong-foam generation is thought to depend on exceeding a threshold pressure gradient or velocity, conditions in these regions might not be favorable for the foam to exist (Ashoori et al. 2012; Yu et al. 2019). We are addressing a hypothetical situation in which foam did not travel far from the wells despite the injection of a sufficient amount of gas and surfactant solution in the reservoir. This work investigates foam generation by snap-off that is triggered by an abrupt permeability and, at that location, capillary-pressure contrast.

In the presence of sharp heterogeneities, foam can be generated by snap-off, independent of pressure gradient or velocity, as gas and surfactant solution flow across an abrupt increase in permeability (Falls et al. 1988; Rossen 1999; Hirasaki et al. 2000; Tanzil et al. 2002a; Li and Rossen 2005; Shah et al. 2018). Fortunately, sharp heterogeneities are quite common in petroleum reservoirs and exist over a large range of length scales. The most prevalent are unconformities such as sharp layer boundaries, which can extend from a few meters to several hundreds of meters in length (Reineck and Singh 1980). Layered systems often consist of internal laminations that add to the frequency of sharp changes in permeability in a given rock volume. Cross laminations present abrupt permeability contrasts in the horizontal direction (Hartkamp-Bakker 1993), offering locations for foam generation by snap-off during lateral pressure-driven flow. Hartkamp-Bakker (1993) measured the permeability variation across internal laminations in a variety of samples extracted from outcrops as well as reservoir cores. She reported permeability ratios across individual units ranging from 1:1 (change in grain framework but not in permeability) to 27:1 between different units.

In flow across such a heterogeneity, the wetting phase accumulates at the boundary of the low-permeability region (Yortsos and Chang 1990) and local capillary pressure is reduced there. If the capillary pressure falls below the critical capillary pressure for snap-off—that is, P_c^{sn} (Falls et al. 1988)—foam generation can be expected. The extreme case of this phenomenon is the capillary end effect encountered in coreflood experiments, which is also reported to have caused foam generation at the outlet of a core (Ransohoff and Radke 1988). Falls et al. (1988) measured the capillary entry pressure (P_c^e) and P_c^{sn} for glass beadpacks using a variety of bead sizes. They found that $P_c^{sn} \approx P_c^e/2$, consistent with theoretical approximations for circular pore throats blocked by snap-off (Roof 1970; Lenormand et al. 1983). Rossen (1999) used this result to show that for snap-off to occur in flow from low- to high-permeability regions, capillary pressure in the high-permeability region must be less than half the capillary pressure in the low-permeability region ($P_c^H < P_c^L/2$). In other words, the high-permeability region is at least four times as permeable as the low-permeability region ($k^H \geq 4\,k^L$), assuming $P_c \propto \sqrt{1/k}$. This trigger for foam generation depends only on the relative magnitudes of capillary pressure resulting from the heterogeneity and not directly on the magnitude of capillary forces in each region. Therefore, for two different gas/liquid fluid pairs, if the liquid is strongly wetting compared with gas, the ratio of capillary pressures is independent of the interfacial tension between the gas/liquid phases because the $P_c(S_w)$ curves would scale but not change shape. This is beneficial for practical applications of foam for displacement processes because the gas available on-site can be used and foam generation in flow across permeability changes can still be expected, assisting with mobility control. The mobilization of the generated foam, however, would depend on the gas/liquid interfacial tension. For instance, as implied earlier, CO_2 foams can propagate at lower pressure gradients compared with N_2 foams.

As the flow gets drier, a greater permeability contrast might be required to cause foam generation. **Fig. 1** shows the calculations of Rossen (1999), in which the permeability contrast required to block gas flow by snap-off (effectively causing foam generation) is plotted as a function of the gas/water relative permeability ratio far from the transition zone in the absence of foam. The relative permeability ratio relates to the injected fractional flow, $f_w = [1 + (k_{rg}/k_{rw})^0(\mu_w/\mu_g)]^{-1}$. Therefore, if $f_g = 80\%$, and $\mu_w/\mu_g = 50$, $(k_{rg}/k_{rw})^0 = 0.08$. According to Fig. 1, a permeability jump slightly higher than 4, at $f_g = 80\%$, would cause foam generation, independent of velocity or pressure gradient. However, if the pore geometry deviates from a circular shape, the ratio of P_c^e/P_c^{sn} might be larger or smaller than 2 (Lenormand et al. 1983; Chambers and Radke 1990; Rossen 2003). As a result, a greater or lower permeability contrast, respectively, might be required to block gas flow by snap-off at the same flowing gas fraction. It is important to note that although capillary pressure falls at the edge of the low-permeability region, gas bubbles are expected to form at the entrance to the high-permeability region. There is no dependency on pressure gradient. However, mobilization of the bubbles and subsequent propagation away from the heterogeneity would require such a driving force.

In this work, foam-generation experiments are conducted by coinjecting surfactant solution and gas at field-like velocities, in a consolidated, sintered-glass porous medium with two layers perpendicular to the direction of flow. Local pressure gradient and saturation maps obtained through X-ray computed tomography are the primary measurements used to identify foam generation and mobilization. The pressure gradient is used to quantify foam strength, whereas local saturation near the permeability contrast is used to quantify the reduction in capillary pressure that causes foam generation. A variety of injection rates and injection fractions are used to validate the threshold conditions for foam generation. The previous work of Shah et al. (2018) on the effect of permeability contrast is extended here to the effect of fractional flow and velocity.

The paper is structured as follows. The next section describes the experimental setup and procedure followed. Then, the outcome of foam-generation experiments conducted at a variety of injection rates and gas fractional flow using a core with a permeability contrast of approximately 3.8:1 are reported in the Results. The Discussion presents an analytical examination of these results, and the main conclusions of this work are provided in the final section.

Experimental Methodology

We conduct coreflooding experiments in a consolidated, sintered-glass core with a low- and high-permeability region, separated by a sharp, monotonic transition (**Fig. 2**). The core is 420 mm in length, with a 165-mm low-permeability region. The low-permeability region has a measured permeability (k^L) of 5.4 ± 0.02 darcies, whereas the high-permeability region has a permeability (k^H) of 20.7 ± 0.2 darcies. Therefore, the permeability contrast k^H/k^L is roughly 3.8:1, bordering the threshold predictions of Rossen (1999). The materials used in this study, together with the experimental protocols followed, are identical to those described in detail by Shah et al. (2018). Nevertheless, we highlight important aspects of the same to ensure independent readability of this manuscript.

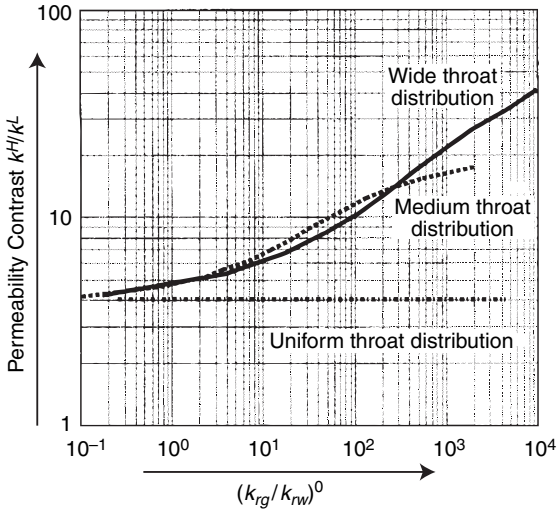

Fig. 1—Theoretically computed permeability contrast required to completely block gas flow as a function of gas/water relative permeability ratio $(k_{rg}/k_{rw})^0$, with the superscript denoting its value far from the transition zone (Rossen 1999). Left to right on the *x*-axis also represents an increase in gas fraction, as $f_w=[1+(k_{rg}/k_{rw})^0(\mu_w/\mu_g)]^{-1}$.

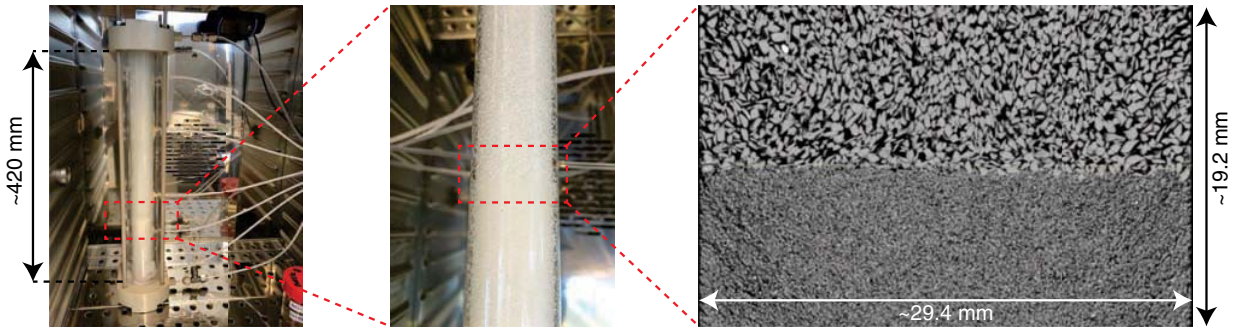

Fig. 2—Core holder (left) with a synthetic sintered-glass core (left and center) and a microCT image of a vertical cross section near the permeability contrast in the core (Shah et al. 2018).

Every experiment begins with multiple permeability measurements using water across the length of the core to ensure that there has been no grain migration and that there is no trapped gas in the core. Next, the core is saturated with brine solution (1 wt% NaCl prepared in demineralized water) and the permeability is measured again. Once the core is saturated with brine, the flow rate is reset to the desired experimental value, and gas (99.98% N_2) is coinjected at the desired fractional flow. After a steady state is achieved with the coinjection of gas and brine, the injected liquid phase is changed to the surfactant solution, and gas and surfactant solution are coinjected into the core. The surfactant solution comprises 0.5 wt% (≈0.04 M) anionic alpha-olefin sulfonate $C_{14–16}$ with a molecular weight of 315 g/mol as the foaming surfactant and 1 wt% (≈0.17 M) NaCl. The surfactant concentration is roughly 62 times the critical micelle concentration in 1 wt% NaCl (Kahrobaei et al. 2017). For a variety of reasons including cost, detergency, and low adsorption on sandstones, alpha-olefin sulfonate is an excellent overall candidate for foam EOR in a conventional, mature oil reservoir (Farajzadeh et al. 2008). Because the experiments are conducted at field-like velocities, foam is not generated in the low-permeability region. Once the surfactant front reaches the permeability transition, foam generation is expected. The core is cleaned thoroughly after each experiment by flushing with 50 wt% isopropanol (IPA) solution for several pore volumes (PVs). IPA is known to kill foams. Therefore, after the core is cleaned with IPA, it is flushed with great amounts (≈20–50 PV) of brine solution. Then, the core is flushed with CO_2 (≈10 PV, with the last 2 PV under vacuum) to displace any remaining gas out of the core, followed by brine again to remeasure permeability before the start of an experiment. This treatment removes all trapped gas, traces of surfactant solution, and IPA from the core. This minimizes chances of hysteresis effects affecting the foam-generation experiments (Kahrobaei et al. 2017).

The experimental procedure followed is similar to the experiments of Li and Rossen (2005). Unlike the experiments of Tanzil et al. (2002a), in which gas and surfactant solution were injected into a surfactant-saturated sandpack, essentially a drainage process, we inject gas and surfactant solution into a core at steady state with gas and brine coinjection. As a result, gas does not drain a surfactant-saturated region of the core before foam generation at the boundary, which ensures that the chances of foam generation by mechanisms that dominate during drainage, such as Roof snap-off (Roof 1970) and leave behind, are minimal (Ransohoff and Radke 1988; Kovscek and Radke 1994; Kovscek et al. 1995; Rossen 1996, 2003). In other words, the experiments were carefully designed not to allow foam generation by mechanisms other than snap-off at the permeability boundary in the core. Once foam is generated at the heterogeneity, gas saturation in the high-permeability region can rise. This can then be considered a local drainage process, and, therefore, other mechanisms of foam generation could come into play as the foam mobilizes and propagates through the high-permeability region.

Fig. 3 shows a schematic flow diagram of the experimental setup. Fig. 2 shows the core in a vertical orientation, whereas in the dual-beam CT scanner, the core is placed horizontally. This is not ideal for flow behavior but is necessary to minimize the impact of beam-hardening effects and cross artifacts while taking CT scans of non-axisymmetrically placed objects. Therefore, gravity segregation affects the experiments conducted using the CT scanner, as discussed by Shah et al. (2018). Along with saturation maps obtained through CT scans, pressure measurements in the low-permeability region are used to confirm that no foam is generated before the

permeability contrast. No backpressure is applied, to avoid fluctuations caused by multiphase flow through the backpressure-regulator assembly. These fluctuations might cause foam generation (Li and Rossen 2005). The image settings for the CT scanner together with the procedure used to analyze CT images are reported by Shah et al. (2018) and reiterated below to ensure independent readability of this manuscript.

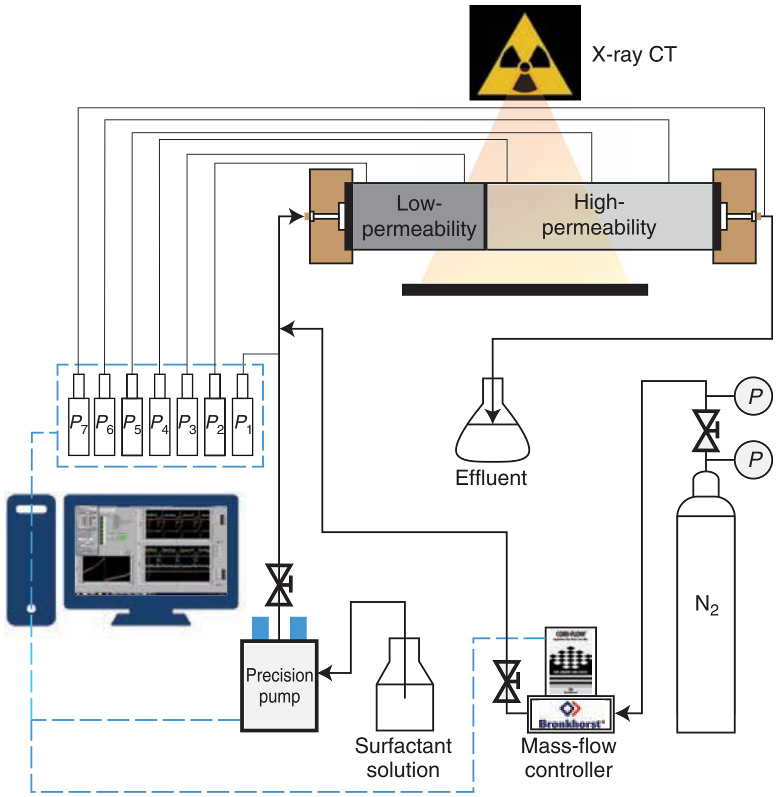

Fig. 3—Schematic of the experimental setup.

A dual-energy CT scanner is used to scan the core in select experiments, to quantify phase saturations through the course of the experiment. A single-energy X-ray beam was sufficient when scanning because the experiments involved a two-phase flow of fluids differing greatly in density. An overview of the applied image settings is reported in **Table 1.** Single-slice helical CT scans were acquired with a pitch of 0.9. A pitch less than 1.0 ensures X-ray beam overlap for the same scanned volume, resulting in better image quality; the lower the pitch, the greater the scan time. These image settings resulted in approximately 260 slices for each scan along the axis of a core, taken over a period of approximately 9 seconds. One slice contains 512 × 512 pixels, a part of which contains the circular core cross section. The images obtained were further processed to compute phase saturations using Fiji (Schindelin et al. 2012), a distribution of the ImageJ software.

Parameter	Setting
Tube voltage	140 KeV
Tube current	250 mA
Pitch	0.9
Slice thickness	1.5 mm
Pixel size	1.5 × 1.5 mm^2
Scan mode	Spiral

Table 1—Overview of settings applied to the CT scanner.

Raw CT data in terms of Hounsfield units are used to compute porosity and phase saturations as a voxel property for each image stack. Porosity can be obtained using the CT scans of a dry and water-saturated core (Mees et al. 2003). During the course of the experiment, liquid-phase saturation is computed for each scan as

$$S_{\text{liq}} = \frac{CT_{\text{exp}} - CT_{\text{dry}}}{CT_{\text{liq}} - CT_{\text{dry}}}, \quad (1)$$

where CT_{exp} denotes the CT measurement taken during the course of the multiphase-flow experiment. CT_{dry} is the CT measurement of a dry core, obtained when the core is not yet saturated with any liquid, before each experiment. CT_{liq} represents the CT measurement for a core that is fully saturated with the liquid phase. In this work, CT_{liq} is measured before the start of each experiment, when the core is fully saturated with brine solution. It is important to note that the accuracy of CT measurements depends on different parameters selected for the X-ray source, such as applied beam voltage, corresponding beam energy, and the applied filters for shaping the beam. Once the liquid-phase saturations are computed for each multiphase scan, a color scheme is applied to the images, where blue represents

the aqueous phase and red represents the gas phase. The images are cropped to include only the circular cross section of the core. In addition, a distance of approximately 2 cm (12 to 13 slices) from the entrance and exit face is excluded from the saturation maps. This is done to avoid any misinterpretation because of the entrance and end effects associated with corefloods. Unusual saturation values also arise near each end of the core because it resides inside the end cap, whereas the rest of the porous medium is only surrounded by the glass tube housing it, as shown in Fig. 2. Phase-saturation maps from select experiments are shown in the next section. The saturation profile across the core can also be obtained by averaging values within each cylindrical image slice. This is also shown in the Discussion section and is used to quantify the local reduction in capillary pressure at the edge of the low-permeability region.

Results

Two sets of experiments are reported in this work. The first set of experiments was conducted with the objective of understanding the impact of superficial velocity on foam generation and mobilization while validating the velocity independence of this process by operating at the lowest injection rates possible within the range of the flow-control equipment. These experiments were conducted at an injected-gas fraction of 80% with the highest total injection rate (q_t) tested being 0.1 cm^3/min, which corresponds to a superficial velocity (u_t) of 2.36 μm/s or 0.67 ft/D in field units. In total, four different injection velocities were considered. Starting at 0.67 ft/D, the rates were successively lowered in each experiment to 0.5 ft/D ($q_t = 0.075\ cm^3$/min), 0.33 ft/D ($q_t = 0.05\ cm^3$/min), and finally to 0.17 ft/D ($q_t = 0.025\ cm^3$/min). The core was placed vertically in a temperature-controlled oven at 30°C to allow for a gravity-stable displacement at the lowest rates considered.

Through the second set of experiments, the effect of fractional flow on foam generation was assessed. Extending the work of Shah et al. (2018), these tests were conducted at $u_t = 0.67$ ft/D. The gas fraction was varied from 60 to 95%. Lower gas fractions are less relevant for field applications and, therefore, have not been reported. These experiments were conducted with the core placed horizontally on the CT-scanner table.

Effect of Velocity. Foam generation was observed at all the tested velocities at $f_g = 80\%$. **Fig. 4a** shows a typical measurement of the pressure gradient across various sections of the core, as indicated in **Fig. 5.** The maximum pressure drop across the core in all experiments is close to 0.5 bar, and the outlet of the core is at atmospheric pressure. Fig. 4a reports pressure gradient for the experiment conducted at $u_t = 0.5$ ft/D, whereas Fig. 4b reports the experiment conducted at the lowest velocity (i.e., $u_t = 0.17$ ft/D). The horizontal axis represents the total PVs of injection (PVI) of surfactant solution and N_2 gas. The core has reached a steady state to gas/brine injection at the origin of the plot.

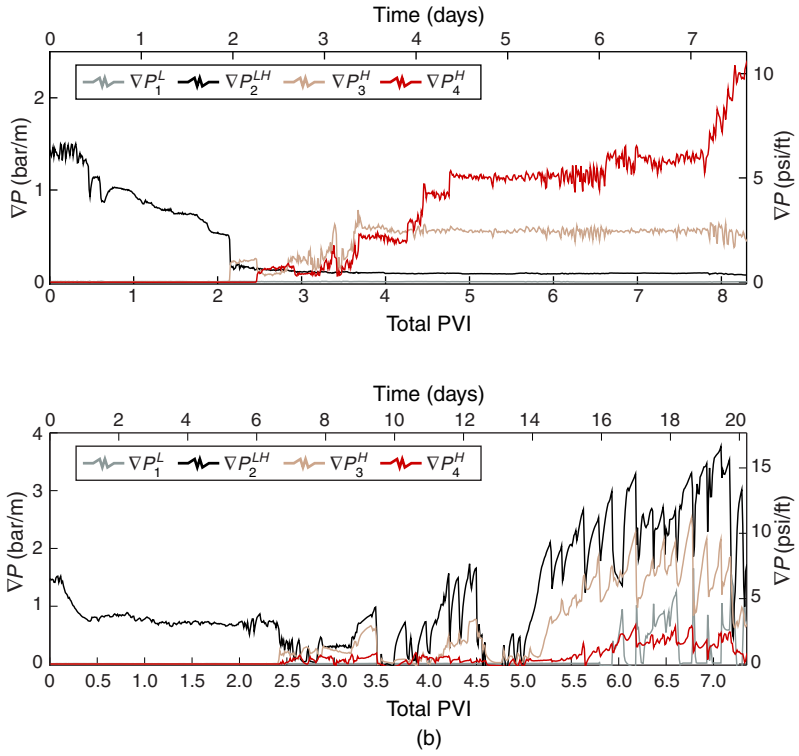

Fig. 4—Pressure gradient across various sections of the core during the foam-generation experiment conducted at (a) $u_t = 0.5$ ft/D and (b) $u_t = 0.17$ ft/D at a fixed gas fractional flow of 80%. Superscript *L* represents a measurement in the low-permeability region, whereas superscript *H* represents data acquired from the high-permeability region. *LH* represents the interval with the boundary.

As mentioned previously, before surfactant is introduced in the core, each experiment starts with gas injection into a brine-saturated core. As gas drains the low-permeability region, the pressure transducers report a jump in pressure, indicating the arrival of gas. If each transducer measures the same phase once gas has arrived at the outlet of the core, then these jumps in absolute pressure correspond to spikes in terms of the pressure gradient. However, in all the experiments conducted, regardless of the orientation of the core, the pressure gradient across the permeability transition ∇P_2^{LH} (black line in Fig. 4) is atypically high for gas/brine injection, and the pressure gradient immediately downstream ∇P_1^L registers a slightly negative value. We believe that this is because of the pressure tap right before the permeability transition sensing a different phase compared with the rest of the ports (McCool et al. 1983; Chen et al. 2016; Shah et al. 2018). Gas trapping and the capillary-pressure contrast within the core might add to this effect. The experimental data reported by As Syukri (2018) during gas/brine flow for similar experiments further support this explanation. As more and more

surfactant is injected, ∇P_2^{LH} gradually declines. When the surfactant arrives at the permeability contrast, foam is generated across the permeability transition. As the foam strength increases, the pressure taps in the high-permeability region sense the reduction in gas mobility starting with the transducer immediately downstream of the transition. This is represented by the sharp drop in ∇P_2^{LH} and jump in ∇P_3^H, at approximately 2.2 total PVI (0.44 PVI liquid) in Fig. 4a and 2.4 total PVI (0.4 PVI liquid) in Fig. 4b. ∇P_4^H rises shortly after. In Fig. 4a, ∇P_4^H rises further into the experiment, at approximately 4.5 PVI total. This corresponds to the passage of foam across the final section in the high-permeability region, followed by its arrival at the outlet of the core.

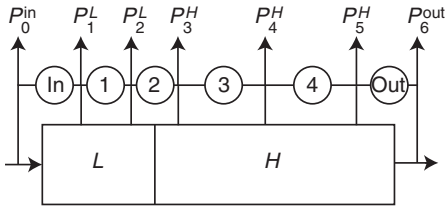

Fig. 5—Schematic showing the labeling scheme used to denote local pressure and pressure gradient.

At the end of the experiment at $u_t = 0.17$ ft/D (Fig. 4b), at approximately 5.9 total PVI, the pressure gradient in the low-permeability region begins to rise. Because ∇P_1^L is low until that point, we can conclude that no strong foam is generated in the low-permeability region before generation at the boundary. No significant rise in ∇P_1^L was observed in any other experiment reported in this paper. Because this experiment is conducted at a lower velocity compared with all the other experiments reported in this paper, in which no such rise in pressure gradient was observed, it is reasonable to conclude that the injection rate was not so high so as to cause foam generation in the low-permeability region unintentionally. We contend that this rise in pressure gradient is because of a secondary, upstream buildup in pressure gradient, indicating an apparent backward propagation of foam, similar to that observed in previous work (Apaydin and Kovscek 2001; Simjoo et al. 2013).

Apaydin and Kovscek (2001) observe a secondary rise in pressure gradient, traversing upstream, after the breakthrough of the initial foam front in their experiments with surfactant concentrations higher than 0.1 wt%. This front propagation against the direction of flow might be originating from increased gas trapping near the outlet of the core. The original generation of stronger foam at the outlet they ascribe to the capillary end effect. The backward propagation begins soon after breakthrough. The time taken to achieve a steady-state pressure profile throughout the core is much larger than in other experiments because the buildup of pressure drop against the direction of flow is a slow process. Simjoo et al. (2013) observed what they called a "secondary desaturation front" traveling from outlet to inlet in their experiments, after breakthrough. In our experiments, we have a finite transition in permeability inside the core, which is effectively an internal capillary end effect. The rise in ∇P_1^L happens after several PVI. In the field, the region around such a heterogeneity might experience several PVs of surfactant and gas. If the surfactant concentrations are high enough (Apaydin and Kovscek 2001) and the velocities are low enough (to allow incremental gas trapping), one can expect foam generation and propagation in the low-permeability regions also.

Not including the case discussed previously, it is important to note that the pressure gradient in the low-permeability region ∇P_1^L is low and does not indicate any reduction in gas mobility because of foam generation upstream of the permeability jump. Comparing Figs. 4a and 4b, it is evident that the magnitude of fluctuations in the pressure gradient is greater at the lower velocity or injection rate. This subject of intermittency of the process shown by fluctuations in pressure gradient will be discussed later in this paper. For the foam-generation experiments conducted at $u_t = 0.67$ ft/D, $u_t = 0.5$ ft/D (Fig. 4a), and $u_t = 0.33$ ft/D, pressure gradient in the final section inside the high-permeability region, ∇P_4^H, is either similar to or greater than ∇P_3^H in magnitude. In these experiments, the strength of foam generated at the permeability transition is maintained as it propagates downstream to the outlet of the core. However, as shown in Fig. 4b, at $u_t = 0.17$ ft/D, ∇P_4^H is lower than ∇P_3^H, indicating a drop in foam strength upon propagation. At this velocity, we reach the limit of foam propagation, and the foam generated at the permeability contrast is unable to steadily reach the outlet of the core. This is confirmed by observations made at the outlet of the core **(Fig. 6).** A typical observation made at the outlet of the core is shown in Fig. 6a for $u_t = 0.33$ ft/D. At this velocity (and higher velocities), steady foam production is observed with infrequent, short, intermittent bursts of only gas and liquid production. At $u_t = 0.17$ ft/D, however, short periods (a few minutes to an hour) of relatively coarse foam production is observed (Fig. 6b), followed by a large amount of gas production (several hours to a day, corresponding to a few PVIs) as shown in Fig. 6c, followed by liquid for a similar time interval, as shown in Fig. 6d.

Fig. 6—(a) Snapshot of the outlet tubing showing fluids produced from the core as a typical observation of steady foam production at $u_t = 0.33$ ft/D. (b) Short bursts of foam production preceded by liquid, (c) a few PVs of gas production, and (d) liquid are observed at $u_t = 0.17$ ft/D.

Effect of Fractional Flow. **Fig. 7** shows two foam-generation experiments performed at the same injection rate but with different fractional flow. The core has been placed horizontally on the medical CT-scanner table. Fig. 7a shows pressure gradient vs PVs injected at $u_t = 0.67$ ft/D and $f_g = 60\%$. The lower horizontal axis represents PVs of surfactant-solution PVI into the core. Close to approximately 1 PVI total or 0.4 PVI liquid, foam generation takes place across the permeability transition indicated by the drop in ∇P_2^{LH} and jump in ∇P_3^H, similar to the experiments reported previously. The dash-dotted lines in the plot indicate times at which CT scans were taken across the core. Foam generation inferred from changes in sectional pressure-gradient measurements is also confirmed through phase-saturation profiles **(Fig. 8).** As explained in the previous section, the saturations are computed using X-ray CT images (Mees et al. 2003), with blue representing a high liquid saturation and red representing a high gas saturation. The images display phase saturation in a vertical cross section through the center of the core. In the image at 0.5 PVI surfactant solution, gas saturation begins to rise in the high-permeability region immediately downstream of the permeability transition. This confirms that the drop in ∇P_2^{LH} and jump in ∇P_3^H mark the onset of foam generation across the permeability contrast. At the start of surfactant injection, we observe an ambiguous buildup in gas saturation near the inlet of the core, as seen in the image at 0.08 PVI liquid. However, this does not correspond to a reduction in gas mobility in terms of pressure gradient because there is no evident rise in ∇P_1^L (gray line in Fig. 7a). This region of high gas saturation does not appear in subsequent CT images, confirming that foam is indeed generated at the permeability transition, seen clearly as a sharp contrast in gas saturation in the CT images. There is no strong foam present in the low-permeability region. After 1.2 PVI surfactant, the foam has propagated downstream from the permeability contrast to the final section in the high-permeability region and ∇P_4^H gradually rises. The experiment is ended soon after 2.2 PVI liquid as foam arrives at the outlet of the core.

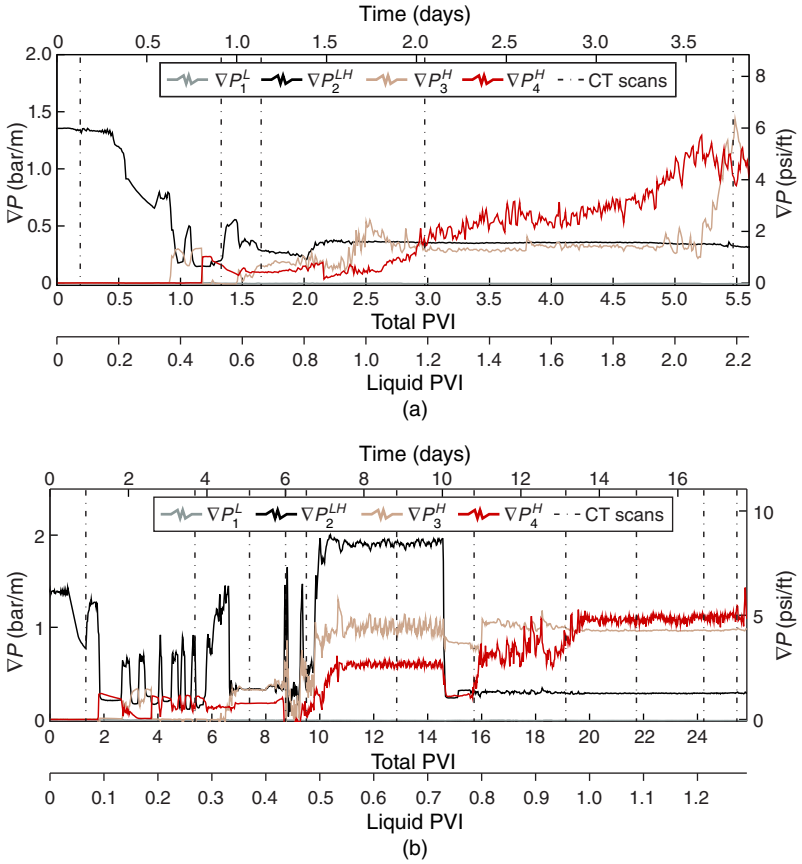

Fig. 7—Pressure gradient across various sections of the core plotted against both total and surfactant (secondary horizontal axis) PVs injected during the foam-generation experiment conducted at (a) $f_g = 60\%$ and (b) $f_g = 95\%$ at a fixed total superficial velocity of 0.67 ft/D. Superscript *L* represents a measurement in the low-permeability region, whereas superscript *H* represents data acquired from the high-permeability region. *LH* represents the interval with the boundary.

Fig. 7b shows pressure gradient vs. PVIs for an experiment performed at the same injection rate ($u_t = 0.67$ ft/D) but a higher injected-gas fraction ($f_g = 95\%$). **Fig. 9** reports phase saturations for this experiment, computed using X-ray CT imaging, as seen in a vertical cross section through the center of the core. Evidently, the pressure gradient across the permeability transition exhibits larger fluctuations while foam arrives at the outlet faster (in terms of liquid injected) compared with the experiment conducted at $f_g = 60\%$. At roughly 0.1 PVI surfactant, the pressure gradient in the high-permeability region appears to rise. In this case, however, it does not mark the onset of foam generation, because the CT image taken at 0.27 PVI liquid does not indicate foam in the high-permeability region. The next CT image, at 0.37 PVI liquid, shows a foam front propagating through the high-permeability region. Therefore, the onset of foam generation is marked by the sharp drop in ∇P_2^{LH} or rise in ∇P_3^H at approximately 0.33 PVI surfactant. Gas saturation in the low-permeability region increases substantially after surfactant is introduced in the core. The CT images at 0.48 PVI liquid and 0.64 PVI liquid show a gas saturation of almost 85% in the low-permeability region, close to the permeability transition. Later in the experiment, the gas saturation is lower, at approximately 60%. The relatively high gas saturation, however, does not correspond to a significant reduction in gas mobility, because ∇P_1^L stays low. Pressure drop in the low-permeability region gradually rises from approximately 1 to 10 mbar through the experiment. The absolute-pressure transducers are accurate up to 3 mbar. This allows for a maximum mobility

reduction by a factor of 16. We think that the relatively high gas saturation in the low-permeability region, in this experiment, is because of the creation of a continuous-gas foam. If the foam were discontinuous, blocked flow paths and moving lamellae would register a higher pressure gradient in the low-permeability region, closer to the measurements in the high-permeability region. Moving lamellae would multiply by lamella division, and this would abruptly increase the pressure gradient as the experiment progressed. Thus, it is a continuous gas phase without moving lamellae that reaches the permeability transition. Nevertheless, strong foam is generated in flow across the permeability transition, and the foam propagates downstream from the heterogeneity toward the outlet of the core.

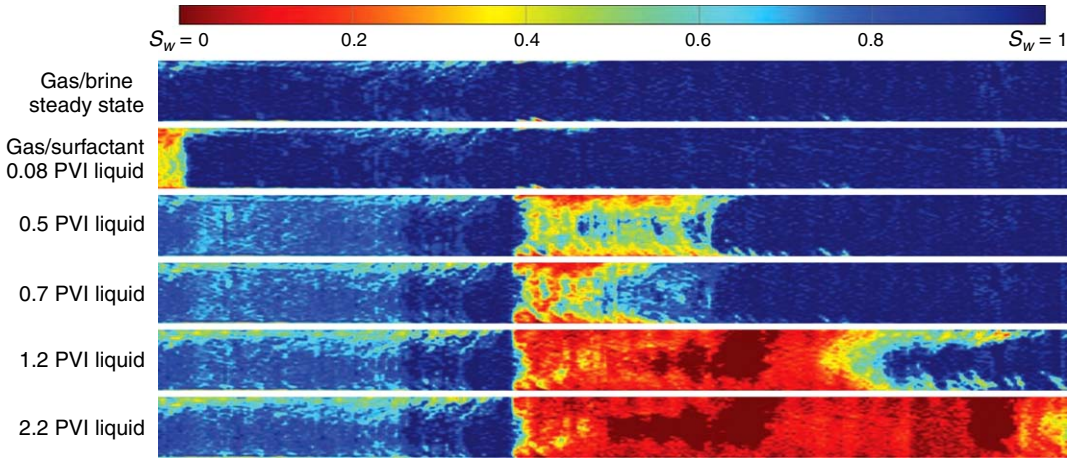

Fig. 8—Average liquid saturation in a vertical cross section through the center of the core obtained using X-ray CT imaging for the foam-generation experiment conducted at $u_t = 0.67$ ft/D and $f_g = 60\%$. The image at the top represents a measurement during steady-state gas/brine coinjection, and the images thereafter were taken at times corresponding to the dashed lines in Fig. 7a. Blue represents a high liquid saturation, while red represents a high gas saturation, as indicated by the color bar at the top.

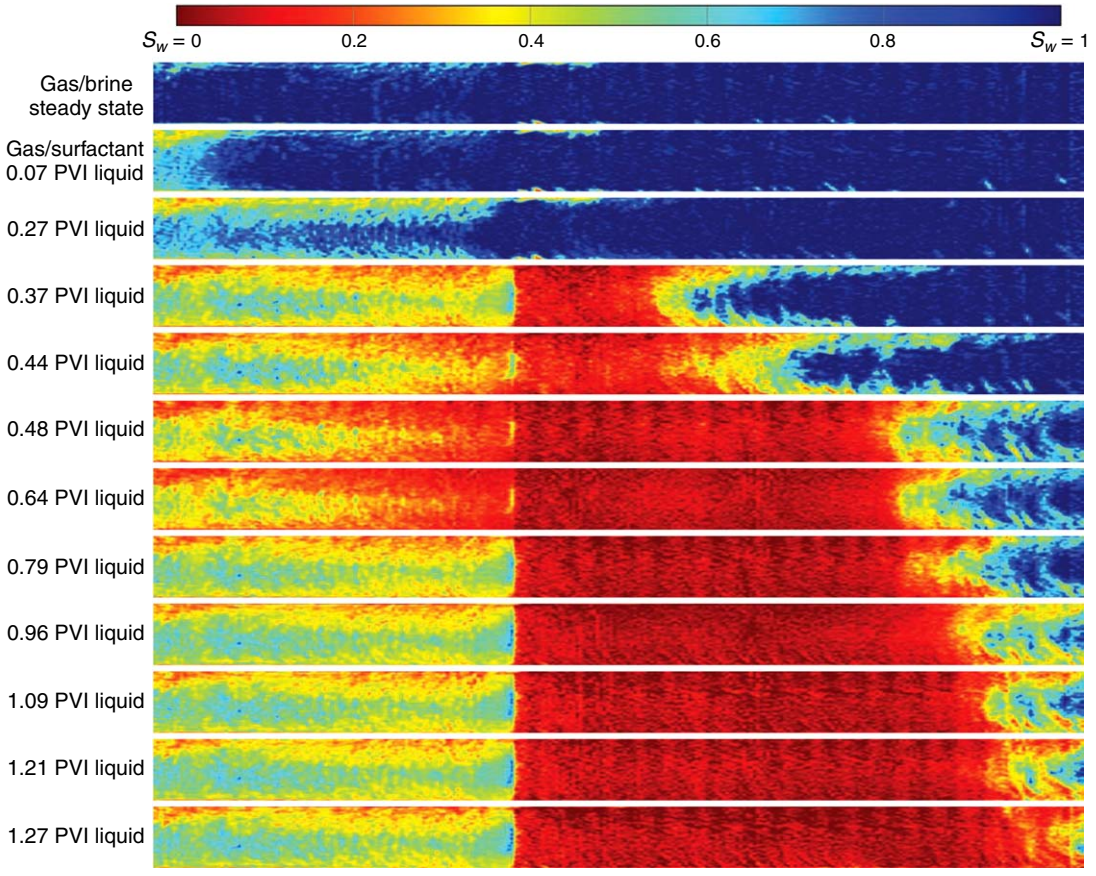

Fig. 9—Average liquid saturation in a vertical cross section through the center of the core obtained using X-ray CT imaging for the foam-generation experiment conducted at $u_t = 0.67$ ft/D and $f_g = 95\%$. The image at the top represents a measurement during steady-state gas/brine coinjection, and the images thereafter were taken at times corresponding to the dashed lines in Fig. 7b. Blue represents a high liquid saturation whereas red represents a high gas saturation, as indicated by the color bar at the top.

In both the experiments reported in Fig. 7, foam generation takes place after similar amounts of liquid injection, which conforms with the expected time of arrival of the surfactant solution at the permeability contrast. However, the pressure response to the same is quite different. The pressure gradient across the permeability contrast exhibits large fluctuations at $f_g = 95\%$. As mentioned previously, when looking at the pressure measurements, it appears that a modest and arguably sporadic resistance to gas flow is witnessed in the high-permeability region long before foam begins to appear in the CT images as a high-gas-saturation front moving through the region. At the end of both experiments, the pressure gradient in the high-permeability region is similar at approximately 1 bar/m. This indicates minimal to no sensitivity to the change in the fractional flow on the final mobility. Experiments conducted at other gas fractions, as reported in the next section, also yielded similar observations. The theory of Rossen (1999) suggests that foam generation by snap-off in flow across a sharp permeability transition is easier in wetter flow. Some other studies indicate that the strength of steady-state foam in a sandstone can be higher during wetter flow (Persoff et al. 1991; Kovscek et al. 1995), whereas Huh and Handy (1989) report the opposite. In this study, with respect to foam generation by snap-off in flow across an abrupt permeability jump, we do not observe significant differences in foam strength or the time at which foam generation commences at lower gas fractions to support the findings of Rossen (1999). For a permeability contrast of approximately 3.8:1, foam generation is observed at higher gas fractions than predicted by theory (Fig. 1).

Discussion

A series of injection rates and gas fractions were used to examine the effect of fractional flow and velocity on foam generation across a sharp permeability contrast of 3.8:1. Foam generation was observed at all the conditions tested. Snap-off in flow of gas and surfactant solution across an abrupt heterogeneity is intermittent in nature (Falls et al. 1988; Shah et al. 2018). Foam is not created steadily across the interface as the surfactant solution reaches the permeability jump. In our experiments, the onset of foam generation, and often the period thereafter, is accompanied by large fluctuations in the measured pressure gradient across the permeability transition and in the high-permeability region. As mentioned earlier, foam generation begins when capillary pressure at the edge of the low-permeability region falls below P_c^{sn}. Snap-off in pore throats blocks the flow of gas, causing the local gas fraction to increase and the flow to become drier. Locally, the capillary pressure might momentarily rise above P_c^{sn} and foam generation stops. Eventually, liquid convects or imbibes back to the boundary of the low-permeability region and accumulates, creating favorable conditions for snap-off. This cycle of events repeats itself, and we think it is responsible for the large fluctuations in pressure gradient observed in our experiments. We observe that this intermittency, in terms of magnitude and frequency of fluctuations in pressure gradient, is greater as the velocity decreases. **Fig. 10** shows the measured pressure gradient across the entire high-permeability region (Fig. 10a) and the corresponding apparent viscosity (Fig. 10b). Each data point represents all the measurements recorded and averaged over 0.05 PVI surfactant solution (or 0.25 total PVI). The error bar in each direction represents one standard deviation of all the measurements within this window, representing the magnitude of fluctuation in pressure gradient. As the injection rate decreases, the magnitude of these fluctuations increases. For each case, the pressure gradient rises after roughly the same amount of liquid injected (≈0.4 PV), corresponding to the time at which the surfactant solution arrives at the permeability contrast.

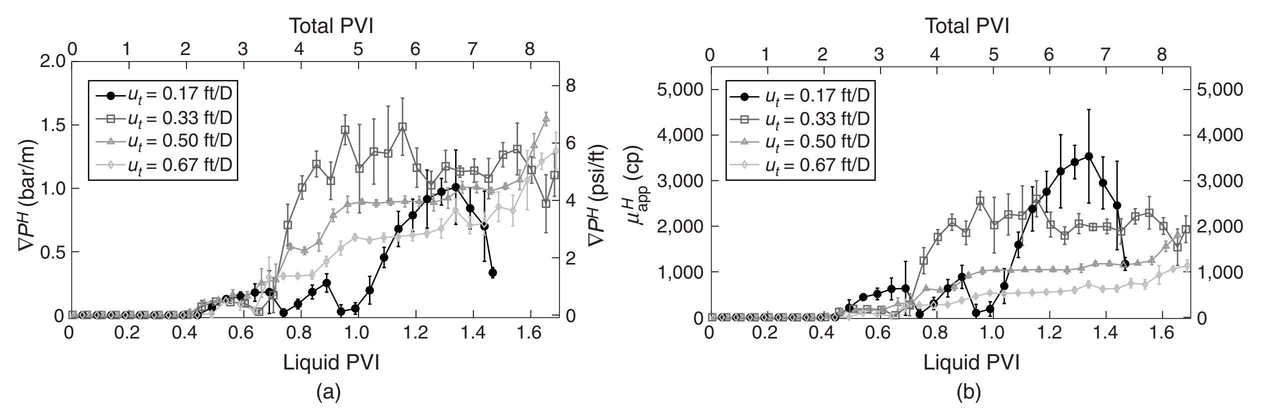

Fig. 10—Pressure gradient measured across the high-permeability region of the core at (a) four different injection rates and (b) corresponding apparent viscosity; $f_g = 80\%$ in all the experiments.

Apparent viscosity is computed as

$$\mu^H_{app} = \frac{k^H \nabla P^H}{u_t}, \quad (2)$$

where k^H is the measured permeability in the high-permeability region, ∇P^H is the pressure gradient across the same section during the experiment, and u_t is the total superficial velocity. Therefore, if the pressure gradient remains the same, the computed apparent viscosity increases with decreasing velocity. While the experiment at $u_t = 0.17$ ft/D records the highest apparent viscosity, the foam does not reach the outlet of the core, as reported in the previous section. Ignoring the experiment at the lowest velocity, Fig. 10a shows that the measured pressure gradient is, for the most part, higher at a lower injection rate. This is counterintuitive for two-phase flow but can be explained as follows: As capillary number (or velocity in this case, because permeability is kept constant) increases, the impact of capillary heterogeneity decreases (Yortsos and Chang 1990). For the same reason, coreflooding experiments are often conducted at high injection rates to minimize the influence of the capillary end effect. Therefore, as velocity in our experiments increases, the rate of foam generation can be affected in such a way that the strength of the resulting foam is reduced. Note that this would hold true only for foam created by snap-off across an abrupt increase in permeability. For other mechanisms of bubble generation, a higher velocity would lead to the creation of a stronger foam. From the results of our experiments, it can be implied that a reduction in gas mobility can be expected far from wells in a foam EOR application, provided that sharp heterogeneities are present in the formation. For all practical

purposes, it can be considered that this phenomenon is independent of velocity. While velocities as low as 0.17 ft/D might never be reached in a typical reservoir setting, we still observe foam generation across a permeability contrast of 3.8:1 at this superficial velocity. At velocities much greater than 1 ft/D, other mechanisms of foam generation come into play and the impact of snap-off across heterogeneities might be less significant.

Experiments with varying gas fractions were conducted with the core placed horizontally on the CT-scanner table. CT images together with pressure measurements were used to identify when foam generation began and whether foam successfully propagated toward the outlet of the core. **Fig. 11** shows a plot of the apparent viscosity in the high-permeability region plotted against PVI surfactant solution for three different fractional flows. Because the total velocity and absolute permeability remain constant between the experiments, the trend in apparent viscosity also reflects the trend in pressure gradient in the high-permeability region. The CT images corresponding to $f_g = 60\%$ and $f_g = 95\%$ are shown in Figs. 8 and 9, respectively. As discussed in the previous section, for the experiments conducted at $f_g = 80\%$ and $f_g = 95\%$, pressure gradient in the high-permeability region rises before the CT images show a high gas saturation in that zone. Therefore, after ≈0.1 PVI liquid, the apparent viscosity (μ^H_{app}) is approximately 100 cp for these experiments (Fig. 11). However, the CT images visualize a foam front that begins to develop and move through the high-permeability region after roughly the same liquid volume has been injected. This observation is independent of f_g, and, as mentioned previously, of u_t. Moreover, the onset of foam generation is accompanied by fluctuations in pressure gradient, which are more frequent, and larger in magnitude in these two experiments compared with the test at $f_g = 60\%$. However, it takes longer (in terms of liquid PVI) for foam to propagate downstream to the outlet of the core at $f_g = 60\%$ compared with the other two experiments. In other words, it takes more surfactant solution for foam at 60% quality to travel the same distance as foam at 95% quality.

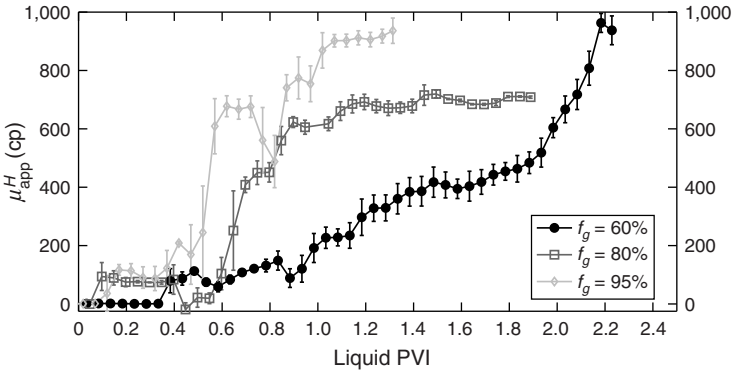

Fig. 11—Apparent viscosity across the high-permeability region of the core through experiments conducted at three different injected-gas fractions with the core placed horizontally in the CT scanner; u_t = 0.67 ft/D in all the experiments.

At the end of the experiments shown in Fig. 11, $\mu^H_{app} \approx 900$ cp for $f_g = 95\%$, 700 cp for $f_g = 80\%$, and 950 cp for $f_g = 60\%$. It is not entirely clear why the foam's apparent viscosity drops at 80% foam quality. It is possible that if the experiment was continued for an extended period of time, the apparent viscosity would reach a similar value. Nevertheless, this observation is inconsistent with the observations of Tanzil et al. (2002a) and Falls et al. (1988), who observed a decrease in pressure gradient and foam apparent viscosity with an increase in gas fraction. In both their experiments, foam was generated across a permeability discontinuity as a combination of gas and surfactant solution drained a medium already saturated with a surfactant solution. Moreover, in the experiments of Tanzil et al. (2002a), a decrease in f_g between successive tests was also accompanied by an increase in u_t, since the gas velocity was kept constant. These differences in experimental protocols might be responsible for the contrast in experimental observations. As Syukri (2018) performed so-called foam-quality-scan experiments (Ma et al. 2013, 2014) with a homogeneous, sintered-glass core with the same permeability as the high-permeability region of the porous medium used in this study. In his foam scans, the foam was generated under drainage conditions by injecting gas and surfactant solution into a surfactant-saturated core. The transition foam quality was 80%, and the foam apparent viscosity was lower at a foam quality of 60 and 95%. The experiments at $f_g = 60\%$ and $f_g = 95\%$ were performed again to ensure repeatability. The experiment at $f_g = 80\%$ and $u_t = 0.67$ ft/D is a replication of an experiment performed by Shah et al. (2018) under identical conditions. The results of all the experiments performed at the same injection conditions were similar, and the previous discussion holds, regardless of which experimental data we select.

To further investigate and validate the theory of foam generation across permeability contrasts by snap-off, we investigate the saturation profile in the core obtained through CT imaging, focusing on the permeability contrast. **Fig. 12** shows the average steady-state liquid saturation in the core plotted against dimensionless core length (x/L). Mean saturation values in the low- and high-permeability regions, and at the transition, are indicated. Every measurement on the graph represents average saturation inside a circular CT image slice, and each slice is 1.5 mm thick, as is the voxel size. Image settings identical to Shah et al. (2018) were applied while scanning the core. The permeability jump in the core takes place over one or, at most two "coarse" grain diameters, equivalent to approximately 0.5 mm. Because the voxel depth is more than this grain size, the CT measurement at the permeability contrast (at $x/L \approx 0.38$ in Fig. 12) defines the average liquid saturation near the edge of the low-permeability region. The exact liquid saturation one pore throat away from the heterogeneity can be higher. Nonetheless, the saturation profile gives a good indication of the behavior across the heterogeneity in terms of liquid accumulation and local reduction in capillary pressure.

Berg et al. (2014) and Armstrong et al. (2016) measured capillary pressure as a function of saturation using mercury-intrusion porosimetry for sintered-glass core plugs, as used in this study. We use the Leverett J-function (Leverett 1941) to extend these measurements to the petrophysical and fluid properties of our experimental system and construct capillary-pressure curves for the two regions in the core. The curves are plotted on a semilog scale in **Fig. 13a.** As indicated in the figure, capillary-pressure curves obtained through mercury-intrusion porosimetry include an entry-slope region. Several authors have investigated the physical meaning of this region (Schowalter 1979; Katz and Thompson 1986; Nabawy et al. 2009). The entry-slope region concerns pore throats near the edges of the porous medium that is being entered by the nonwetting phase. It is not representative of drainage in the bulk of the porous medium. Therefore, we estimate the capillary entry pressure of the low-permeability region by extending the P_c curve (ignoring the entry-slope

region) to intersect with the vertical line representing a water-saturated core ($S_w = 1$), indicated by the dashed arrow in Fig. 13a. Note that to model snap-off across a permeability change, however, imbibition-type capillary-pressure curves must be used, which include the entry-slope region that allows capillary pressure to reach the critical value for snap-off at effective gas saturations between zero and unity. Drainage capillary-pressure curves would not allow for this type of snap-off because P_c is always higher than P_c^e anywhere on the drainage P_c vs. S_w curve (Falls et al. 1988). Even when occurring in a macroscopic drainage process, snap-off results from a brief moment of local imbibition into appropriately sized pore constrictions that meet the strictly geometric criteria for static snap-off (Roof 1970; Ransohoff and Radke 1988; Chambers and Radke 1990), which is a temporary deviation from drainage behavior, in its exact sense.

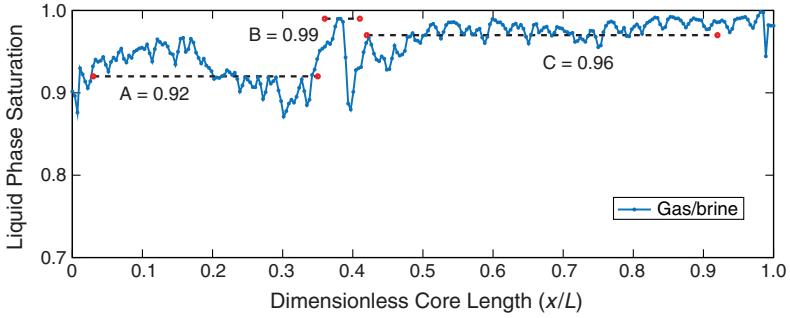

Fig. 12—Steady-state liquid-saturation profile across the core during gas/brine coinjection. Dotted lines indicate average saturation in the low-permeability region, at the transition, and in the high-permeability region.

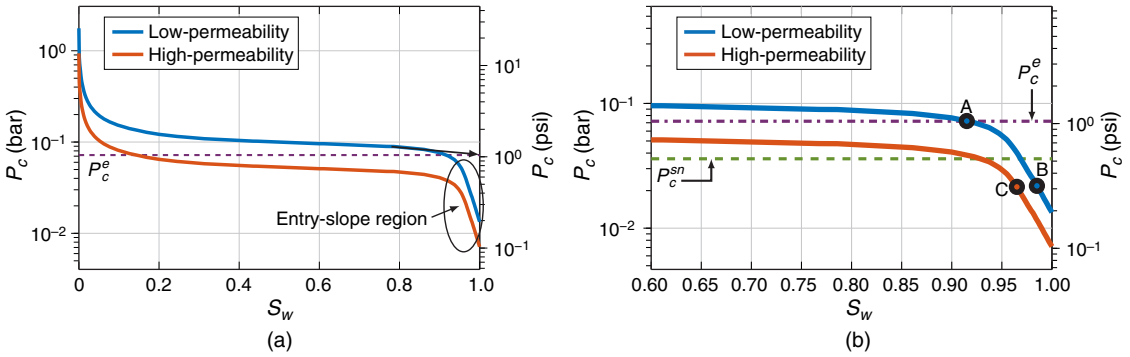

Fig. 13—(a) Capillary-pressure curves for the high- and low-permeability regions in the core extracted from the measurements of Berg et al. (2014) and adjusted to the petrophysical and fluid properties of our system, and (b) capillary pressure corresponding to average liquid saturations indicated in Fig. 12.

In Fig. 13b, the capillary-pressure curve is magnified close to the liquid-saturated end. The average liquid saturations indicated in Fig. 12 are plotted on the curve. $P_c^{sn} = \frac{1}{2} P_c^e$ is assumed (Falls et al. 1988) and marked by the green dashed line on the plot. The capillary pressure corresponding to the average saturation in the low-permeability region (Point A in Fig. 13b) is just above the entry pressure of the region. At the transition, liquid accumulates to maintain capillary continuity, and it can be seen that the capillary pressure drops to below the capillary pressure for snap-off (Point B). The capillary pressure corresponding to the average liquid saturation in the high-permeability region (Point C) is close to P_c at the transition. In alignment with the theory of Yortsos and Chang (1990), this response indicates that the permeability contrast is sharp and monotonic. Moreover, because the P_c at the transition is lower than P_c^{sn}, snap-off is observed as surfactant is introduced into the system. This is consistent with the work of Rossen (1999) and Falls et al. (1988). A similar investigation can be followed in all the experiments performed with CT-assisted saturation measurements, and it is observed that capillary pressure at the boundary of the low-permeability region drops below the critical capillary pressure for snap-off, resulting in foam generation across the permeability contrast. A complete analysis of the path followed along the P_c curve would include the edge effect on the measured drainage capillary-pressure curves in Fig. 13a and the effect of imbibition on the low-permeability region at the boundary.

As mentioned previously, the observations from the experiment conducted at $u_t = 0.67$ ft/D and $f_g = 95\%$ show that, for a given permeability contrast, foam was generated at a higher gas fraction than expected (Fig. 1). This disagreement with the work of Rossen (1999) could arise from the fact that Rossen used a pore-network model with the effective-medium approximation (Kirkpatrick 1973) to compute relative permeability and model flow in homogeneous regions. For the porous medium used in this study, the flow behavior is different, and the relative permeabilities of the gas and liquid phases allow for the saturation response shown in Fig. 12. As a result, the reduction in P_c is sufficient to cause snap-off even at $f_g = 95\%$.

Conclusions

Experiments at low superficial velocities were conducted with a variety of fractional flows in a layered core to observe foam generation by snap-off. In reservoirs where the geological setting allows for the presence of sharp changes in permeability, snap-off can help reduce gas mobility away from wells in which the superficial velocities are low. These heterogeneities can exist in the form of layer

boundaries or laminations and cross laminations within individual layers. The permeability changes can be parallel or perpendicular to the direction of flow, or a combination of the two. When the contrast is parallel to the direction of flow, upward migration of gas because of gravity can cause foam generation in the high-permeability layers. Once foam is generated, gas mobility in the vertical direction will be reduced, effectively increasing the segregation length (Stone 1982; Jenkins 1984; Rossen and van Duijn 2004) and improving sweep efficiency in the low-permeability layers. In the presence of lateral changes in permeability, snap-off can help maintain foam strength and improve the mobility control deep inside the formation. Foam generation across sharp permeability contrasts can have important consequences for foam EOR applications, and it must be taken into account for the improvement in overall sweep efficiency.

In this study, foam generation was observed almost immediately as the surfactant solution arrives at the permeability contrast, irrespective of f_g or u_t. However, in our synthetic porous medium, surfactant adsorption is almost negligible, and in a more realistic setting, adsorption must first be satisfied before foam generation commences. In agreement with the observations of Falls et al. (1988), snap-off across the permeability contrast was an intermittent process. This is best indicated by periods of a fluctuating pressure gradient that mark the onset of foam generation and subsequent propagation. This intermittency, in terms of magnitude and frequency of fluctuations in pressure gradient, was greater at higher gas fractions and lower velocities. The saturation maps constructed using CT imaging for some of our experiments help confirm that foam was indeed generated at the permeability transition and from there it propagates downstream to the end of the core. The saturation maps also show that the local reduction in capillary pressure near the permeability jump is consistent with previous theory (Falls et al. 1988; Yortsos and Chang 1990; Rossen 1999).

Nomenclature

k = absolute permeability, m^2
k_{rg} = gas relative permeability
k_{rw} = liquid (water or surfactant solution) relative permeability
L = core length, m
P_c = capillary pressure, Pa
$\bigtriangledown P$ = pressure gradient, Pa/m
q = flow rate, cm^3/min
S = phase saturation
u = superficial (Darcy) velocity, m/s
x = distance along the core, m
μ = viscosity, cp

Superscripts

e = entry pressure, used to denote capillary entry pressure for a porous medium
L = low-permeability region
LH = region with low- to high-permeability transition
H = high-permeability region
min = minimum, used to denote minimum $\bigtriangledown P$ or velocity required to generate foam
sn = snap-off, used to denote critical capillary pressure required for snap-off
0 = used to denote a property (e.g., relative permeability) away from the permeability transition in the absence of foam

Subscripts

app = apparent
dry = CT measurement of the dry core
exp = CT measurement of the core during the foam-generation experiment
g = gas
l = liquid
liq = CT measurement of the liquid-saturated core
t = total

Acknowledgments

This paper is a result of a collaboration between Delft University of Technology and Universiti Teknologi Petronas. We thank Petronas and Shell for funding this research. We gratefully acknowledge Michiel Slob, Ellen Meijvogel-de Koning, Marc Friebel, Karel Heller, and Jolanda van Haagen-Donker for their extensive technical support at the Laboratory of Geoscience and Engineering of Delft University of Technology.

References

Almajid, M. M. and Kovscek, A. R. 2016. Pore-Level Mechanics of Foam Generation and Coalescence in the Presence of Oil. *Adv Colloid Interface Sci* **233:** 65–82. https://doi.org/10.1016/j.cis.2015.10.008.

Almajid, M. M. and Kovscek, A. R. 2019. Pore Network Investigation of Trapped Gas and Foam Generation Mechanisms. *Transp Porous Media*. https://doi.org/10.1007/s11242-018-01224-4.

Apaydin, O. G. and Kovscek, A. R. 2001. Surfactant Concentration and End Effects on Foam Flow in Porous Media. *Transp Porous Media* **43** (3): 511–536. https://doi.org/10.1023/A:1010740811277.

Armstrong, R. T., McClure, J. E., Berrill, M. A. et al. 2016. Beyond Darcy's Law: The Role of Phase Topology and Ganglion Dynamics for Two-Fluid Flow. *Phys Rev E* **94** (4): 043113. https://doi.org/10.1103/PhysRevE.94.043113.

Ashoori, E., Marchesin, D., and Rossen, W. 2012. Multiple Foam States and Long-Distance Foam Propagation in Porous Media. *SPE J.* **17** (4): 1231–1245. SPE-154024-PA. https://doi.org/10.2118/154024-PA.

As Syukri, H. 2018. *Experimental Study: Foam Generation and Propagation in Flow Across a Permeability Contrast*. Master's thesis, Delft University of Technology, Delft, The Netherlands. http://resolver.tudelft.nl/uuid:961bf2b5-28d5-41e4-9283-a20e1c5d672b.

Berg, S., Armstrong, R., Ott, H. et al. 2014. Multiphase Flow in Porous Rock Imaged Under Dynamic Flow Conditions With Fast X-Ray Computed Microtomography. *Petrophysics* **55** (4): 304–312. SPWLA-2014-v55n4a3.

Chambers, D. J. 1994. Foams for Well Stimulation. In *Foams: Fundamentals and Applications in the Petroleum Industry,* ed. L. L. Schramm, Vol. 242 of *Advances in Chemistry,* Chap. 9, 355–404. Washington, DC: American Chemical Society. https://doi.org/10.1021/ba-1994-0242.ch009.

Chambers, K. and Radke, C. 1990. Capillary Phenomena in Foam Flow through Porous Media. In *Interfacial Phenomena in Oil Recovery,* ed. N. Morrow, Vol. 36 of *Surfactant Science Series,* Chap. 6, 191–256. New York: Marcel Dekker, Inc.

Chen, M., Yortsos, Y., and Rossen, W. 2005. Insights on Foam Generation in Porous Media From Pore-Network Studies. *Colloids Surf A* **256** (2–3): 181–189. https://doi.org/10.1016/j.colsurfa.2005.01.020.

Chen, X., Kianinejad, A., and DiCarlo, D. A. 2016. An Extended JBN Method of Determining Unsteady-State Two-Phase Relative Permeability. *Water Resour Res* **52** (10): 8374–8383. https://doi.org/10.1002/2016WR019204.

Dake, L. P. 1994. The Practice of Reservoir Engineering. In *Developments in Petroleum Science*, Vol. 36. Amsterdam, The Netherlands: Elsevier.

Falls, A., Hirasaki, G., Patzek, T. et al. 1988. Development of a Mechanistic Foam Simulator: The Population Balance and Generation by Snap-Off. *SPE Res Eng* **3** (3): 884–892. SPE-14961-PA. https://doi.org/10.2118/14961-PA.

Farajzadeh, R., Krastev, R., and Zitha, P. 2008. Foam Films Stabilized With Alpha-olefin Sulfonate (AOS). *Colloids Surf A* **324** (13): 35–40. https://doi.org/10.1016/J.COLSURFA.2008.03.024.

Friedmann, F., Chen, W., and Gauglitz, P. 1991. Experimental and Simulation Study of High-Temperature Foam Displacement in Porous Media. *SPE Res Eng* **6** (1): 37–45. SPE-17357-PA. https://doi.org/10.2118/17357-PA.

Gauglitz, P. A., Friedmann, F., Kam, S. I. et al. 2002. Foam Generation in Homogeneous Porous Media. *Chem Eng Sci* **57** (19): 4037–4052. https://doi.org/10.1016/S0009-2509(02)00340-8.

Gupta, D. V. S. 2009. Unconventional Fracturing Fluids for Tight Gas Reservoirs. Paper presented at the SPE Hydraulic Fracturing Technology Conference, The Woodlands, Texas, USA, 19–21 January. SPE-119424-MS. https://doi.org/10.2118/119424-MS.

Hartkamp-Bakker, C. 1993. *Permeability Heterogeneity in Cross-Bedded Sandstones: Impact on Water/Oil Displacement in Fluvial Reservoirs*. PhD dissertation, Delft University of Technology, Delft, The Netherlands. http://resolver.tudelft.nl/uuid:be8ffa8f-5b66-4c46-932b-56d3eab5823e.

Hirasaki, G. J., Jackson, R. E., Jin, M. et al. 2000. Description of Surfactant/Foam Process and Surfactant-Enhanced Aquifer Remediation. In *NAPL Removal: Surfactants, Foams, and Microemulsions*, ed. S. Fiorenza, C. Miller, C. Oubre, and C. Ward, Chap. 1, 7–10, Boca Raton: AATDF Monograph Series, CRC Press.

Hirasaki, G. J., Miller, C. A., Szafranski, R. et al. 1997a. Field Demonstration of the Surfactant/Foam Process for Aquifer Remediation. Paper presented at the SPE Annual Technical Conference and Exhibition, San Antonio, Texas, USA, 5–8 October. SPE-39292-MS. https://doi.org/10.2118/39292-MS.

Hirasaki, G. J., Miller, C. A., Szafranski, R. et al. 1997b. Surfactant/Foam Process for Aquifer Remediation. Paper presented at the International Symposium on Oilfield Chemistry, Houston, Texas, USA, 18–21 February, 471–480. SPE-37257-MS. https://doi.org/10.2118/37257-MS.

Huh, D. and Handy, L. 1989. Comparison of Steady and Unsteady-State Flow of Gas and Foaming Solution in Porous Media. *SPE Res Eng* **4** (1): 77–84. SPE-15078-PA. https://doi.org/10.2118/15078-PA.

Jenkins, M. 1984. An Analytical Model for Water/Gas Miscible Displacements. Paper presented at the SPE Enhanced Oil Recovery Symposium, Tulsa, Oklahoma, USA, 15–18 April. SPE-12632-MS. https://doi.org/10.2118/12632-MS.

Kahrobaei, S., Vincent-Bonnieu, S., and Farajzadeh, R. 2017. Experimental Study of Hysteresis Behavior of Foam Generation in Porous Media. *Sci Rep-UK* **7** (1): 1–9. https://doi.org/10.1038/s41598-017-09589-0.

Kam, S. and Rossen, W. R. 2003. A Model for Foam Generation in Homogeneous Media. *SPE J.* **8** (4): 417–425. SPE-87334-PA. https://doi.org/10.2118/87334-PA.

Katz, A. J. and Thompson, A. H. 1986. Quantitative Prediction of Permeability in Porous Rock. *Phys Rev B* **34** (11): 8179–8181. https://doi.org/10.1103/PhysRevB.34.8179.

Kharabaf, H. and Yortsos, Y. C. 1998. A Pore-Network Model for Foam Formation and Propagation in Porous Media. *SPE J.* **3** (1): 42–53. SPE-36663-PA. https://doi.org/10.2118/36663-PA.

Kirkpatrick, S. 1973. Percolation and Conduction. *Rev Mod Phys* **45** (4): 574–588. https://doi.org/10.1103/RevModPhys.45.574.

Kovscek, A. R., Patzek, T. W., and Radke, C. J. 1995. A Mechanistic Population Balance Model for Transient and Steady-State Foam Flow in Boise Sandstone. *Chem Eng Sci* **50** (23): 3783–3799. https://doi.org/10.1016/0009-2509(95)00199-F.

Kovscek, A. R. and Radke, C. J. 1994. Fundamentals of Foam Transport in Porous Media. In *Foams: Fundamentals and Applications in the Petroleum Industry*, ed. L. Schramm, Vol. 242 of *Advances in Chemistry,* Chap. 3, 115–163, Washington, DC: American Chemical Society. https://doi.org/10.1021/ba-1994-0242.ch003.

Kovscek, A. R. and Radke, C. J. 1996. Gas Bubble Snap-Off Under Pressure-Driven Flow in Constricted Noncircular Capillaries. *Colloids Surf A* **117** (1–2): 55–76. https://doi.org/10.1016/0927-7757(96)03637-0.

Kovscek, A. R. and Radke, C. J. 2003. Pressure-Driven Capillary Snap-Off of Gas Bubbles at Low Wetting-Liquid Content. *Colloids Surf A* **212** (2–3): 99–108. https://doi.org/10.1016/S0927-7757(02)00302-3.

Lenormand, R., Zarcone, C., and Sarr, A. 1983. Mechanisms of the Displacement of One Fluid by Another in a Network of Capillary Ducts. *J Fluid Mech* **135:** 337–353. https://doi.org/10.1017/S0022112083003110.

Leverett, M. 1941. Capillary Behavior in Porous Solids. *J Pet Technol* **142** (1): 152–169. SPE-941152-G. https://doi.org/10.2118/941152-G.

Li, Q. and Rossen, W. R. 2005. Injection Strategies for Foam Generation in Homogeneous and Layered Porous Media. Paper presented at the SPE Annual Technical Conference and Exhibition, Dallas, Texas, USA, 9–12 October. SPE-96116-MS. https://doi.org/10.2118/96116-MS.

Lyons, W. C., Guo, B., Graham, R. L. et al. 2009. *Air and Gas Drilling Manual*, third edition. Amsterdam, The Netherlands: Elsevier. https://doi.org/10.1016/B978-0-12-370895-3.X0001-6.

Ma, K., Farajzadeh, R., Lopez-Salinas, J. L. et al. 2014. Non-Uniqueness, Numerical Artifacts, and Parameter Sensitivity in Simulating Steady-State and Transient Foam Flow through Porous Media. *Transp Porous Med* **102** (3): 325–348. https://doi.org/10.1007/s11242-014-0276-9.

Ma, K., Lopez-Salinas, J. L., Puerto, M. C. et al. 2013. Estimation of Parameters for the Simulation of Foam Flow through Porous Media. Part 1: The Dry-Out Effect. *Energy Fuels* **27** (5): 2363–2375. https://doi.org/10.1021/ef302036s.

McCool, C. S., Parmeswar, R., and Willhite, G. P. 1983. Interpretation of Differential Pressure in Laboratory Surfactant/Polymer Displacements. *SPE J.* **23** (5): 791–803. SPE-10713-PA. https://doi.org/10.2118/10713-PA.

Mees, F., Swennen, R., Geet, M. V. et al. 2003. Applications of X-Ray Computed Tomography in the Geosciences. *Geol Soc Spec Publ* **215:** 1–6. https://doi.org/10.1144/GSL.SP.2003.215.01.01.

Nabawy, B. S., Géraud, Y., Rochette, P. et al. 2009. Pore-Throat Characterization in Highly Porous and Permeable Sandstones. *Am Assoc Pet Geol Bull* **93** (6): 719–739. https://doi.org/10.1306/03160908131.

Persoff, P., Radke, C. J., Pruess, K., et al. 1991. A Laboratory Investigation of Foam Flow in Sandstone at Elevated Pressure. *SPE Res Eval & Eng* **6** (3): 365–372. SPE-18781-PA. https://doi.org/10.2118/18781-PA.

Ransohoff, T. and Radke, C. 1988. Mechanisms of Foam Generation in Glass-Bead Packs. *SPE Res Eng* **3** (2): 573–585. SPE-15441-PA. https://doi.org/10.2118/15441-PA.

Reineck, H. E. and Singh, J. B. 1980. *Depositional Sedimentary Environments*. Berlin, Heidelberg: Springer Berlin Heidelberg. https://doi.org/10.1007/978-3-642-96291-2.

Roof, J. G. 1970. Snap-Off of Oil Droplets in Water-Wet Pores. *SPE J.* **10** (1): 85–90. SPE-2504-PA. https://doi.org/10.2118/2504-PA.

Rossen, W. R. 1990a. Minimum Pressure Gradient for Foam Flow in Porous Media: Effect of Interactions With Stationary Lamellae. *J Colloid Interface Sci* **139** (2): 457–468. https://doi.org/10.1016/0021-9797(90)90118-8.

Rossen, W. R. 1990b. Theory of Mobilization Pressure Gradient of Flowing Foams in Porous Media. I. Incompressible Foam. *J Colloid Interface Sci* **136** (1): 17–37. https://doi.org/10.1016/0021-9797(90)90075-Y.

Rossen, W. R. 1996. Foams in Enhanced Oil Recovery. In *Foams: Theory, Measurements and Applications*, eds. R. K. Prud'homme and S. A. Khan, Vol. 57 of *Surfactant Science Series*, Chap. 11, 413–464. New York: Marcel Dekker. https://doi.org/10.1201/9780203755709.

Rossen, W. R. 1999. Foam Generation at Layer Boundaries in Porous Media. *SPE J.* **4** (4): 409–412. SPE-59395-PA. https://doi.org/10.2118/59395-PA.

Rossen, W. R. 2003. A Critical Review of Roof Snap-Off as a Mechanism of Steady-State Foam Generation in Homogeneous Porous Media. *Colloids Surf A* **225** (1–3): 1–24. https://doi.org/10.1016/S0927-7757(03)00309-1.

Rossen, W. R. and Gauglitz, P. A. 1990. Percolation Theory of Creation and Mobilization of Foams in Porous Media. *AIChE J* **36** (8): 1176–1188. https://doi.org/10.1002/aic.690360807.

Rossen, W. R. and van Duijn, C. J. 2004. Gravity Segregation in Steady-State Horizontal Flow in Homogeneous Reservoirs. *J Pet Sci Eng* **43** (1–2): 99–111. https://doi.org/10.1016/J.PETROL.2004.01.004.

Schindelin, J., Arganda-Carreras, I., Frise, E. et al. 2012. Fiji: An Open-Source Platform for Biological-Image Analysis. *Nat Methods* **9** (7): 676–682. https://doi.org/10.1038/nmeth.2019.

Schowalter, T. T. 1979. Mechanics of Secondary Hydrocarbon Migration and Entrapment. *Am Assoc Pet Geol Bull* **5** (149): 723–760. https://doi.org/10.1306/2F9182CA-16CE-11D7-8645000102C1865D.

Shah, S. Y., Wolf, K.-H., Pilus, R. et al. 2018. Foam Generation by Capillary Snap-Off in Flow Across a Sharp Permeability Transition. *SPE J.* **24** (1): 116–128. SPE-190210-PA. https://doi.org/10.2118/190210-PA.

Simjoo, M., Dong, Y., Andrianov, A. et al. 2013. CT Scan Study of Immiscible Foam Flow in Porous Media for Enhancing Oil Recovery. *Ind Eng Chem Res* **52** (18): 6221–6233. https://doi.org/10.1021/ie300603v.

Stone, H. L. 1982. Vertical, Conformance in an Alternating Water-Miscible Gas Flood. Paper presented at the SPE Annual Technical Conference and Exhibition, New Orleans, Louisiana, USA, 26–29 September. SPE-11130-MS. https://doi.org/10.2118/11130-MS.

Tanzil, D., Hirasaki, G. J., and Miller, C. A. 2002a. Mobility of Foam in Heterogeneous Media: Flow Parallel and Perpendicular to Stratification. *SPE J.* **7** (2): 203–212. SPE-78601-PA. https://doi.org/10.2118/78601-PA.

Tanzil, D., Hirasaki, G. J., and Miller, C. A. 2002b. Conditions for Foam Generation in Homogeneous Porous Media. Paper presented at the SPE/DOE Improved Oil Recovery Symposium, Tulsa, Oklahoma, USA, 13–17 April. SPE-75176-MS. https://doi.org/10.2118/75176-MS.

Yang, J. and Siddiqui, S. 1999. The Use of Foam to Improve Liquid Lifting from Low-Pressure Gas Wells. Paper presented at the Petroleum Conference of the South Saskatchewan Section, Regina, Saskatchewan, Canada, 18–21 October. PETSOC-99-126. https://doi.org/10.2118/99-126.

Yortsos, Y. C. and Chang, J. 1990. Capillary Effects in Steady-State Flow in Heterogeneous Cores. *Transp Porous Media* **5** (4): 399–420. https://doi.org/10.1007/BF01141993.

Yu, G., Vincent-Bonnieu, S., and Rossen, W. 2019. Foam Propagation at Low Superficial Velocity: Implications for Long-Distance Foam Propagation. Paper presented at the IOR 2019–20th European Symposium on Improved Oil Recovery, Pau, France, 8–11 April. https://doi.org/10.3997/2214-4609.201900108.

Swej Y. Shah is a PhD degree candidate at the Department of Geoscience and Engineering, Delft University of Technology, The Netherlands. His current research interests include foam-generation mechanisms in porous media, population-balance models for modeling foam behavior, and multiscale methods for reservoir simulation. Shah holds a BS degree in chemical engineering from the Institute of Chemical Technology in Mumbai, India, and an MS degree in applied earth sciences from Delft University of Technology.

Herru As Syukri is an MS-degree graduate in applied Earth sciences from Delft University of Technology. His interests are in foam generation and propagation in flow across a permeability contrast. As Syukri holds a BS degree in petroleum engineering from Bandung Institute of Technology, Indonesia.

Karl-Heinz Wolf is an associate professor of petrophysics in the Department of Geoscience and Engineering at Delft University of Technology. He works on the interfaces between geology, reservoir engineering, and geophysics, and develops petrophysical techniques for laboratory-scale rock-texture characterization/quantification. Wolf's interests also include clean coal technologies, in-situ oil (shale) combustion, and CO_2 enhanced coalbed methane. He holds a PhD degree in applied Earth sciences from Delft University of Technology.

Rashidah Mohd Pilus is a senior lecturer and the deputy head of the Department of Petroleum Engineering at Universiti Teknologi Petronas, Malaysia. She holds a BS degree from the University of Nebraska, Omaha; an MS degree from McMaster University, Canada; and a PhD degree from Queens University, Belfast, Northern Ireland, all in chemistry.

William R. Rossen is a professor of reservoir engineering in the Department of Geoscience and Engineering, Delft University of Technology. His current research concerns the use of foams for diverting fluid flow in porous media, modeling complex transport processes in networks, and understanding flow in naturally fractured geological formations. Rossen is an SPE Distinguished Member.